# Scattering Model-Based Oil-Slick-Related Parameters Estimation From Radar Remote Sensing: Feasibility and Simulation Results

Tingyu Meng, *Associate Member, IEEE*, Ferdinando Nunziata, *Senior Member, IEEE*, Xiaofeng Yang, *Senior Member, IEEE*, Andrea Buono, *Senior Member, IEEE*, Kun-Shan Chen, *Fellow, IEEE*, and Maurizio Migliaccio, *Fellow, IEEE*

***Abstract*— In this study, the potential of electromagnetic scattering models to retrieve quantitative parameters of sea oil spills is investigated using an artificial intelligence (AI)-based approach. The backscattering coefficient of a slick-covered sea surface is predicted using the advanced integral equation model augmented with the model of local balance (MLB), an effective dielectric constant model, and a composite medium model to include the effect of an oil slick. Damping ratios (DRs), predicted for different oil parameters (namely, the oil thickness and seawater volume fraction), are used to train and test a four-layer neural network. Once successfully tested, the neural network is applied to an uninhabited aerial vehicle synthetic aperture radar (UAVSAR) image collected during the DeepWater Horizon (DWH) oil spill accident to retrieve the oil slick thickness and volume fraction of seawater in the oil layer. The inversion results show that the thicker (i.e., 2–4 mm) emulsions are located in the south and west of the slick and they are surrounded by thinner (i.e., <1 mm) oil films. In addition, the seawater volume fraction in the oil slick is found to be about 20%–30%. Results are contrasted with optical data and previous studies of the same accidental oil spill, showing qualitatively good agreement.**

***Index Terms*— Artificial neural network (ANN), DeepWater Horizon (DWH), oil spill, parameter inversion, scattering model, synthetic aperture radar (SAR).**

Manuscript received 5 December 2023; revised 18 January 2024; accepted 7 February 2024. Date of publication 23 February 2024; date of current version 6 March 2024. This work was supported in part by the National Key Research and Development Program of China under Grant 2021YFB3901300, in part by the European Space Agency (ESA)-National Remote Sensing Center of China (NRSCC) Dragon-5 Cooperation Project under Grant 57979, in part by the China Scholarship Council, and in part by the Agenzia Spaziale Italiana (ASI) under the APPLICAVEMARS Project within the framework of the call DC-UOT-2019-017 under Contract 2021-4-U.0. *(Corresponding author: Xiaofeng Yang.)*

Tingyu Meng is with the National Key Laboratory of Microwave Imaging Technology, Aerospace Information Research Institute, Chinese Academy of Sciences, Beijing 100190, China (e-mail: mengty@radi.ac.cn).

Ferdinando Nunziata and Andrea Buono are with the Dipartimento di Ingegneria, Università degli Studi di Napoli "Parthenope," 80143 Naples, Italy (e-mail: ferdinando.nunziata@uniparthenope.it; andrea.buono@uniparthenope.it).

Xiaofeng Yang is with the State Key Laboratory of Remote Sensing Science, Aerospace Information Research Institute, Chinese Academy of Sciences, Beijing 100101, China, and also with the Institute of Space Earth Science, Nanjing University, Suzhou Campus, Suzhou 215163, China (e-mail: yangxf@radi.ac.cn).

Kun-Shan Chen is with the Institute of Space Earth Science, Nanjing University, Suzhou Campus, Suzhou 215163, China (e-mail: chenks@radi.ac.cn).

Maurizio Migliaccio is with the Dipartimento di Ingegneria, Università degli Studi di Napoli "Parthenope," 80143 Naples, Italy, and also with the Sezione Osservazione della Terra, Istituto Nazionale di Geofisica e Vulcanologia, 00143 Rome, Italy (e-mail: maurizio.migliaccio@uniparthenope.it).

Digital Object Identifier 10.1109/TGRS.2024.3369023

## I. Introduction

THE synthetic aperture radar (SAR) is unanimously recognized as a key operational remote sensing instrument for oil spill surveillance and damage assessment owing to its all-day and almost all-weather observation ability together with its fine spatial resolution. Although SAR sea oil slick surveillance is a mature enough application [1], the estimation of ancillary information as the oil thickness and fractional volume of seawater is still a challenging task [2]. After crude oil is spilled into the marine environment, it spreads over the sea surface and, under the action of wind and waves, typically starts to mix with seawater giving rise to an emulsion layer underneath the oil film [3]. Thick layers can be formed for fresh-spilled crude oils or emulsions with their thickness ranging from micrometer to millimeter and even centimeter in the case of low sea state [4]. The spatial extent of the oil and its thickness distribution are pivotal parameters for remediation purposes that drive the choice of the more suitable response method and the spatial allocation of response resources. Thick or emulsified oil, which needs to be contained, dispersed, burned, or recovered for clean-up work or prosecution, has the thickness of 0.5–10 mm [5], [6]. In these cases, the knowledge of thickness and volume fraction of oil in the water column is required to target the thickest oil layer or the water area with the highest oil concentration [7].

However, the accurate and reliable estimation of the oil thickness and the percentage of oil dispersed into the seawater remain difficult tasks [8]. In fact, nowadays, operational oil thickness estimation is performed by trained personnel who visually inspect the oil slick with the aid of optical cameras. Empirical relationships between the visual appearance of an oil slick and its thickness have been proposed, among which the most extensively adopted is the one included in the Bonn Agreement [9]. Nevertheless, the visual estimation of the oil film thickness depends on subjective and environmental factors. In addition: 1) the estimation approach included in the Bonn Agreement saturates when oil slicks are thicker than 0.1 mm, which is the case that includes emulsified oils requiring clean-up operations [10]; 2) the range of oil thickness visually inspected is orders of magnitude below the relevant thickness ranges needed for oil spill countermeasures to work correctly [2]; and 3) water-in-oil emulsions may differ from nonemulsified oils in both appearance and physical properties

leading to incorrect oil thickness estimations [6]. All this matter suggests that the existing operational methodology to estimate oil thickness is not mature enough and there is still large room for improvement [2].

Recent studies demonstrate the potential of SAR imagery to provide information about the physical properties of oil slicks, namely, thickness and water-in-oil fraction [11], [12]. In the SAR image plane, oil slicks are detected as dark spots since they have lower brightness compared to slick-free sea surfaces. This is due to both geometrical and dielectric effects of the oil slick, which, one on side, damps the short-gravity and capillary sea waves resulting in a lower backscattered signal and, on the other side, if thick or emulsified slicks are in place, the dielectric properties of the upper sea surface can be altered in a way that can be observed at microwave frequencies [8]. To extract information about the oil slick from SAR imagery while limiting effects of sea state conditions and incidence angle, the damping ratio (DR), i.e., the slick-free-to-slick-covered backscattering ratio, has been widely adopted [7], [11], [13], [14], [15], [16], [17], [18], [19]. It has been shown that thick crude oils or emulsified oils may give rise to larger DR values than those of thinner oils. In [20], the DR is estimated over heavy and light fuel oils and it is shown to be largest for heavy fuel oils and it increases with the thickness of the oil layer. In [21], a significant reduction of the backscatter signal is observed in the thickest part of the oil slick. In [11], the DR is exploited as a proxy of oil slick thickness, with larger DR values being related to thicker oil layers. The DR metric is also used to infer the percentage of oil-in-water. In [15] and [16], DR values obtained from L-band uninhabited aerial vehicle SAR (UAVSAR) data collected over the DeepWater Horizon (DWH) polluted area are analyzed to estimate the oil/water mixing ratio. Experimental results show that the oil volume fraction is about 65%–90%. Accordingly, different DR-based metrics are proposed to determine the relative oil slick thickness [7]. In [22], the DR evaluated using co-polarized TerraSAR-X measurements is shown to well-correlate with the oil volume released on the seawater oil under low-to-moderate wind speed. Despite automatic or semiautomatic methods to evaluate the DR of an oil slick [23], [24], SAR-based oil thickness estimation is still far from being a mature application using DR [25].

A key issue that limits the development of robust and effective methodologies to retrieve oil thickness from SAR imagery is the lack of field measurements and validation data [2]. In [3] and [26], the DR is used to estimate the concentration of oil within an oil-in-water emulsion. Numerical predictions, performed using the universal weighted curvature approximation (UWCA) surface scattering model, are contrasted with high-quality [i.e., high signal-to-noise ratio (SNR)] L-band SAR measurements collected during an oil spill clean-up exercise. Although no ground information was available, the estimated thickness is shown to be consistent with the expected behavior of the released oil. In [15] and [16], the DR is used to evaluate the oil concentration in the DWH slick based on the tilted Bragg scattering model. The spilled oil is estimated to be a mixture of approximately 20% seawater and 80% oil whose thickness is at least a few millimeters. These studies open new perspectives for quantitative monitoring of marine oil slicks by dual-polarization SAR imagery [3]. In literature, to the best of our knowledge, there is no study addressing a simultaneous quantitative retrieval of oil thickness and seawater (or oil) volume fraction in the oil slick using the DR metric ingested in an artificial neural network (ANN) processing, i.e. using a model-based ANN approach.

Recently, artificial intelligence (AI) technology has been widely trialed for ability to perform flexible input–output nonlinear mappings between remotely sensed data and geophysical parameters, which has been applied, among all, to retrieve ocean water depth [27] and soil moisture [28] and to predict precipitation [29] and agricultural yield [30]. It has been found great potential for revolutionizing data analysis and application in the field of quantitative remote sensing [31], [32]. In [33], the thickness of DWH oil spill has been retrieved utilizing ANN, which reveals the thickness distribution of the oil slick present on the SAR image. Nevertheless, since the spilled oil appeared highly emulsified characteristics, more information about the emulsion oil is desired to be obtained from SAR measurements.

In this article, an inversion method is proposed to retrieve oil parameters, i.e., oil thickness and fractional volume of seawater simultaneously, from SAR measurements by exploiting an AI strategy. The rationale consists of overcoming the lack of ground information using a forward scattering model (FSM). Hence, first, the backscattered signals from slick-free and oil-covered sea surface are predicted using an FSM specialized to the case of thick oil emulsion [34] and, then, they are combined according to the DR metric. The inversion of oil parameters is carried out by the AI technique that is trained and validated on simulated data obtained from the forward model. Finally, the inversion method is verified using UAVSAR data collected during the DWH oil accident to demonstrate the effectiveness of the proposed approach to estimate oil thickness and water-in-oil volume fraction. Inversion results are qualitatively compared with optical camera images acquired during the DWH accident and visually inspected by trained personnel.

The remainder of this article is organized as follows. The forward model used to predict sea surface scattering with and without thick emulsified oil slicks is introduced in Section II, while the AI-based inversion methodology is outlined in Section III. The UAVSAR and ancillary data collected during the DWH oil spill accident are introduced in Section IV, while the experimental results relevant to the inversion of oil parameters are presented in Section V. Conclusions are drawn in Section VI.

## II. Forward Scattering Model

Several scattering models have been proposed in literature to predict the microwave signal scattered off a randomly rough surface. Those methods can be either numerical or analytical, with the former being typically computational demanding in the case of large scattering media. Hence, a good tradeoff between accuracy and computer-time effectiveness is provided by analytical methods. Among the latter class, the advanced

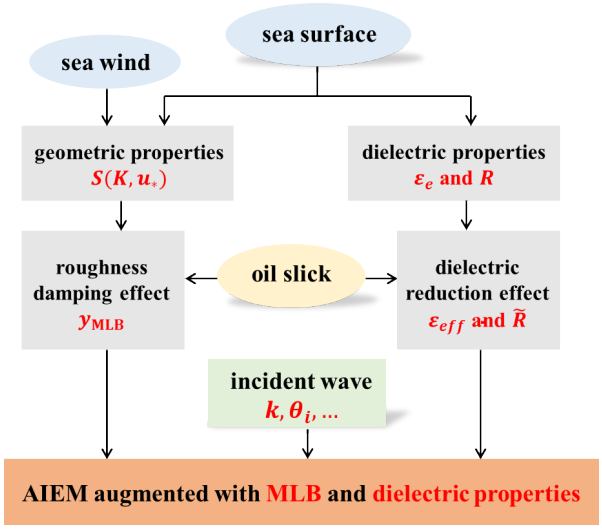


Fig. 1. Flowchart of the FSM for predicting the backscattering from oil-covered sea surfaces.

integral equation method (AIEM), i.e., an improved version of the well-known integral equation method (IEM), has been extensively used to deal with sea surface scattering with and without surfactant in both monostatic and bistatic geometries [12], [34], [35], [36].

In this study, the FSM, depicted in the schematic of Fig. 1, employs the AIEM augmented with a damping model and a model to deal with the effective dielectric constant of the oil/water layer and its effects on the Fresnel reflection coefficients Those models are described in Sections II-A–II-C.

### A. Rough Surface Scattering Model: AIEM

For multiscale roughness surfaces, e.g., the sea surface, the family of two-scale models is largely adopted to include in the predicted normalized radar cross section (NRCS) the effects of both large- and small-wave structures. Among these models, the AIEM has been largely employed since it does not rely on splitting the roughness spectrum into different parts [37], [38]. The AIEM integrates the classical Kirchhoff approximation (KA)—used to describe the scattering contributions resulting from large-scale roughness—with the small perturbation model (SPM)—adopted to describe the scattering contributions resulting from small-scale roughness. The AIEM includes KA and SPM as special cases achieved in the low- and the high-frequency regions of the sea surface roughness spectrum, respectively. By bridging the gap between KA and SPM, the AIEM can be used to predict the NRCS of a sea surface calling for a broad range of roughness. According to the AIEM, the surface field consists of the sum of a Kirchhoff term and a complementary field term. In this way, the NRCS can be obtained as the sum of the Kirchhoff term $\sigma_{pq}^{k}$, the complementary term $\sigma_{pq}^{c}$, and the cross term $\sigma_{pq}^{kc}$ [37]

$$\sigma_{pq}^{0} = \sigma_{pq}^{k} + \sigma_{pq}^{c} + \sigma_{pq}^{kc} \tag{1}$$

where subscripts $p$ and $q$ denote the transmitted and received polarization of the microwave signal, respectively. Given small slopes of typical sea surfaces, the multiple scattering can be neglected and the NRCS of the sea surface predicted by AIEM is given by

$$\sigma_{pq}^{0} = \frac{k^2}{2} e^{-\sigma^2(k_{sz}^2 + k_{iz}^2)} \sum_{n=1}^{\infty} \frac{\sigma^{2n}}{n!} \left| I_{pq}^{n} \right|^2 W^n \tag{2}$$

where $k$ is the wavenumber of the electromagnetic wave with $k_{sz}$ and $k_{iz}$ being the projection of the scattering wave and incident wave on the normal direction. For backscattering configuration, since the scattering angle $\theta_i$ is identical to the incidence angle $\theta_s$, $k_{sz}$ equals $k_{iz}$. $I_{pq}^{n}$ denotes the surface field function, which can be referred to [37] for details. Roughness parameters of the sea surface include: 1) $\sigma$, the root-mean-square (rms) height, and 2) $W^n$, the $n$-fold convolution of the sea surface spectrum, which is also the Fourier transform in the spatial domain of the $n$th power of the autocovariance function $\rho(r, \varphi)$. For sea surfaces, $\sigma$ can be calculated from the omnidirectional sea spectrum $S(K)$ as

$$\sigma^2 = \int_0^{\infty} S(K) dK \tag{3}$$

with $K$ being the wavenumber of sea waves. The functions $\rho(r, \varphi)$ and $W^n$ can be calculated from the directional sea spectrum $S(K, \phi)$ as

$$\rho(r, \varphi) = \frac{1}{\sigma^2} \int_0^{\infty} \int_0^{2\pi} S(K, \phi) \exp(jKr\cos(\varphi - \phi)) K dK d\phi \tag{4}$$

$$W^n(K, \phi) = \frac{1}{2\pi} \int_0^{\infty} \int_0^{2\pi} \rho^n(r, \varphi) \exp(jKr\cos(\varphi - \phi)) r dr d\varphi \tag{5}$$

with $\phi$ being the wind direction with respect to the incident direction of radar. Note that the directional sea surface spectrum $S(K, \phi)$ is factorized into the product of $S(K)$ and the angular spreading function $\Phi(K, \phi)$ as

$$S(K, \phi) = S(K) \cdot \Phi(K, \phi). \tag{6}$$

In this study, $S(K)$ and $\Phi(K, \phi)$ are the ones described in [39].

To predict the scattering from an oil-covered sea surface, the slick-free sea surface AIEM scattering model should be augmented to describe two oil-related effects: 1) the damping of small-scale wind-induced surface waves and 2) the reduction of the sea surface dielectric constant when a thick or emulsified oil is in place [16]. The two effects are described and modeled in Sections II-B and II-C. The backscattered signal, and therefore information retrieval process, also depends on the penetration depth of the radar signal into the mixture that is given by [40]

$$\delta = \frac{1}{k \left| I\left(\sqrt{\varepsilon_{\text{eff}}}\right) \right|} \tag{7}$$

where $I(\cdot)$ stands for imaginary part and $\varepsilon_{\text{eff}}$ is the dielectric constant of the oil/water mixture. The oil—in the microwave range of the spectrum—calls for a dielectric constant, which is relatively much lower than the (typical) sea surface one. According to [40], the intensity of the radar signal reduces

to about 37% of its value at the upper boundary of the layer at $\delta$ meters within the scattering layer. This means that, from an electromagnetic viewpoint, two factors play a key role in the radar sensitivity to oil thickness: the damping and the modification of the dielectric constant.

A thin film (thickness lower than roughly $\delta/10$ [8]) only marginally affects the dielectric constant of the underlying water and, therefore, it does not have any "measurable" effect on the effective dielectric constant of the scattering surface. In this case, the "measurable" effect relies on the attenuation of the NRCS due to the damping of the small-scale Bragg-resonant roughness.

In a thicker layer (thickness larger than roughly $\delta/10$), the radar signal interacts with the medium composed by oil and seawater and, therefore, at least in principle, the backscattered wave carries out information about oil thickness.

The abovementioned theoretical rationale suggests that the radar ability to provide information about the thickness of the mixture layer depends on the radar frequency (according to (7), the higher the frequency, the lower the penetration depth), the dissipation term (i.e., the imaginary part of the dielectric constant), with the larger being the dissipation term and the lower the penetration depth. In addition, the retrieval performance significantly relies on the SAR figure of merit—among them, the noise equivalent sigma zero (NESZ) plays a key role in sea state conditions [41], [42].

### B. Damping of Sea Surface Roughness

The oil slick damps capillary and short-gravity waves through the reduction of wind friction velocity and surface tension, which both suppress wave growth and increase wave viscous dissipation [43]. In addition, the longer wave part can be also affected through nonlinear wave–wave interaction [44]. To include these aspects comprehensively, the model of local balance (MLB) is adopted, which is based on the action balance equation. Accordingly, the damping of sea waves by an oil slick is given by [34]

$$y_{\mathrm{MLB}}\left(u_{*,s}, y_{\mathrm{vis}}[d, \nu_s], \Delta\alpha, K\right) = \frac{\beta\left(u_{*,s}\right) - 2(\Delta \cdot y_{\mathrm{vis}})c_g + (\alpha + \Delta\alpha)}{\beta(u_*) - 2\Delta c_g + \alpha} \tag{8}$$

where $\beta$ denotes the wind growth rate that depends on the wind friction velocity $u_*$. In the case of the slick-covered sea surface, the friction velocity is reduced with respect to the slick-free one by a damping factor $\mu \approx 0.7$–$0.8$. Hence, $u_{*,s} = \mu \cdot u_*$. The viscous dissipation term $2\Delta \cdot c_g$, with $c_g$ being the group velocity of sea waves and $\Delta$ being the clean sea surface damping coefficient, is enhanced in the case of slick-covered surface by the viscous damping coefficient $y_{\mathrm{vis}}$.

In the case of the thick emulsified oil, the two-layer fluid model is here adopted, which relates the viscous damping coefficient $y_{\mathrm{vis}}$ with the thickness $d$, oil viscosity $\nu_s$, and other physical parameters of the finite layer covered on the sea surface [45]. Experimental results have proved that the viscous damping of emulsions (with a thickness spanning from several tenths to 10 mm) can be well described by $y_{\mathrm{vis}}$ [46]. The reduction of the wind input energy $\beta(u_{*,s})$ and the increasing of viscous dissipation $2(\Delta \cdot y_{\mathrm{vis}})c_g$ in the capillary and the short-gravity wave regions of the sea spectrum make the energy transfers from the longer to the shorter wave part to maintain the equilibrium of the sea surface. This is accounted for using the nonlinear wave–wave interactions rate $\alpha$ that is increased with a factor $\Delta\alpha$. Further details about MLB are provided in [34].

The sea surface geometry is described by the roughness spectrum $S(K, u_*)$, i.e., the Fourier transform of the auto-correlation sea surface function. Hence, the slick-covered sea roughness spectrum, $S_s(K, u_{*,s})$, is described by applying the MLB coefficient to the Elfouhaily sea spectrum [39]

$$S_s(K, u_{*,s}, d, \nu_s) = \frac{S(K, u_*)}{y_{\mathrm{MLB}}\left(K, u_{*,s}, d, \nu_s\right)}. \tag{9}$$

The roughness parameter required for the scattering prediction using (2), namely, $\sigma$ and $W^n$, are, therefore, both obtained by the slick-covered sea roughness spectrum $S_s(K, u_{*,s}, d, \nu_s)$.

### C. Reduction of Dielectric Constant for Oil Emulsion

In the microwave region, the dielectric constant of seawater (e.g., $\varepsilon_r \approx 72 - j73$ at L-band) calls for both real and imaginary parts larger than the corresponding crude oil one (which is roughly equal to $\varepsilon_o = 2.3 - j0.02$). However, the mixing of seawater and oil, namely, the oil-in-water emulsion, leads to significant variations in the sea surface dielectric properties. The effective dielectric constant of an oil emulsion can be described by the Bruggeman mixing formula [47]

$$\varepsilon_{\mathrm{eff}}(f_v) = \frac{\varepsilon_e}{4} - (1 - 3f_v)(\varepsilon_i - \varepsilon_e) + \sqrt{\left[\varepsilon_e - (1 - 3f_v)(\varepsilon_i - \varepsilon_e)\right]^2 + 8\varepsilon_i\varepsilon_e} \tag{10}$$

where $f_v$ stands for the fraction of volume that contains homogeneous spherical inclusions, whose dielectric constant is $\varepsilon_i$, while $\varepsilon_e$ denotes the dielectric constant of the host homogeneous environment. In this study, water-in-oil (W/O) emulsions are considered, where seawater droplets (i.e., the inclusions) are surrounded by the oil. In this way, $f_v$ is the seawater volume fraction of the emulsion oil, when $f_v = 0$ (1), the pure crude oil (pure seawater) case is in place.

In addition, the emulsion-covered sea surface is modeled as a composite medium, which consists of three layers: air, finite oil layer, and semi-infinite seawater. The effective reflection coefficient $\tilde{R}$ can be calculated based on the layered medium model

$$\tilde{R}(d, \varepsilon_{\mathrm{eff}}) = \frac{R_{01} + R_{12}e^{-2\gamma_1 d\cos\theta_1}}{1 + R_{01}R_{12}e^{-2\gamma_1 d\cos\theta_1}} \tag{11}$$

where $R_{01}$ and $R_{12}$ (are the reflection coefficients) at the air–oil and the oil–water interfaces, which are both related to the effective dielectric properties of the oil layer $\varepsilon_{\mathrm{eff}}$, and, therefore, they depend on the fraction of seawater in the oil, $f_v$. $\gamma_1$ and $\theta_1$ are the propagation constant and the refraction angle of the electromagnetic wave in the oil layer, respectively, which are both referred to [48]. Note that $R_{01}$ and $R_{12}$ are both related to the permittivity of the oil layer, namely, $\varepsilon_{\mathrm{eff}}$. The composite reflection coefficient is derived from the reflection and transmission of incident waves in the air–oil surface and

oil–seawater interface and is thus suitable for the oil layer with arbitrary thickness.

In this way, the roughness damping effect of oil slicks is embodied through (9) and thus alters $\sigma$ and $W^n$ in (2), which mainly depends on $d$. Also, the effect of dielectric reduction modifies $I^n_{pq}$ in (2) by (10) and (11), which involves both $d$ and $f_v$. By augmenting the AIEM slick-free scattering model including the damping effect and dielectric properties of the oil slick, the NRCS of a slick-covered sea surface, $\sigma^{0,s}_{pq}$, can be predicted. Accordingly, the DR can be predicted as follows [49]:

$$\mathrm{DR}_{pq} = \frac{\sigma^0_{pq}}{\sigma^{0,s}_{pq}}. \tag{12}$$

Fig. 2 shows the L-band DR values predicted at horizontal transmit–horizontal receive (HH) and vertical transmit–vertical receive (VV) polarizations with respect to oil thickness (in mm) and volume seawater fraction (in percentage) at the incidence angle of 30°, under a moderate wind speed of 5 $\mathrm{ms}^{-1}$. Fig. 2(a) shows that the VV-polarized DR is slightly larger than the HH one (less than 0.5 dB), which is consistent with [16] and [50]. Fig. 2(b) and (c) shows that the DR increases monotonically with the oil layer thickness, while it calls for a nonmonotonic trend with respect to the water content. In addition, the DR exhibits the largest sensitivity to $f_v$ at higher $d$ values, while the largest sensitivity to $d$ is at $f_v$ values around 50%. Note that the nonzero DR values for the largest $f_v$ seawater volume fraction are due to the presence of the nonemulsified oil layer.

It is also worth noting that the DR, which can be measured according to (12), carries on key information about both dielectric (which, at once, depend directly on the W/O volume fraction and indirectly on oil thickness) and geometrical (i.e., the surface roughness) properties of the oil slick.

## III. ANN-Based Retrieval Approach

The theoretical model and the sensitivity analysis provided in Section II have shown the nonlinear and implicit relationship between the quantitative parameters of oil slicks and SAR backscattering signals, which requires the inversion method to fulfill the nonlinear modeling capability. ANNs' nonlinear, sample-based, and model-free architecture allow it to solve the highly nonlinear multiparameter relationship between oil parameters and backscattering signals. Therefore, in this section, the retrieval of the oil layer thickness and seawater volume fraction is addressed using an ANN-based inversion scheme, which is applied to simulated SAR measurements.

The proposed retrieval approach consists of three steps: 1) simulating the training dataset using the forward electromagnetic scattering model; 2) training the neural network to optimize its structure and parameter settings; and 3) testing the neural network using an independent simulated test dataset. These steps will be detailed in the following.

In this study, the FSM-ANN technique is implemented to simulate DR values under different incidence angles and oil parameters. The need for using simulated data is due to the lack of consistent and reliable in situ NRCS measurements over slick-covered sea surface. The multilayer perceptron (MLP) is here adopted since, among ANN-based approaches, it is found to be one of the best solutions for nonlinear regression of remotely sensed measurements [51]. The MLP consists of multiple layers whose basic units are known as neurons. The first layer, i.e., the input layer, is separated from the last layer, i.e., the output one, by hidden layers.

TABLE I
Statistics of Oil Parameters and Incidence Angle Used to Simulate the DR Using the FSM ($n = 6000$)

| Variable | Mean | Std | Min | Max |
|---|---|---|---|---|
| $d$ (mm) | 2.99 | 1.16 | 1.00 | 5.00 |
| $f_v$ (%) | 49.79 | 28.85 | 0.00 | 99.99 |
| $\theta_i$ (°) | 49.85 | 7.45 | 37.24 | 63.03 |

The neural network is trained using the slick-free and slick-covered NRCSs predicted using the abovementioned FSM. The weights and bias of the ANN are iteratively adjusted during the training process to minimize the error between the network and forward model output. Finally, the trained ANN is validated by an independent set of model-predicted data.

### A. Training Dataset Simulated by the FSM

To fully train and test the inversion model, the FSM is used to generate a large dataset of simulated DRs. In this study, the goal is to show the ability of the proposed approach to retrieve oil parameters by SAR imagery. Hence, a well-known oil spill is considered, i.e., the DWH accident, and therefore, the external environmental parameters (wind speed $u_*$ and wind direction $\varphi_w$) and rheological properties of oil slicks (viscosity $\nu_s$, surface tension, and so on) are given as fixed input parameters. The values assigned to the oil variables $d$ and $f_v$, as well as the incidence angle $\theta_i$, are randomly generated based on the uniform and independent distribution. $N = 6000$ sets of input variables are generated and the corresponding co-polarized DRs are predicted by the FSM. In this study, the simulated dataset is randomly split into training (3600 sets, 60%) and validation (2400 sets, 40%) datasets. To improve the reliability of the oil parameter retrieval, the oil thickness is constrained in the range of 1–5 mm. The statistics of the FSM simulated dataset are listed in Table I.

### B. Architecture and Training of the ANN

In this study, it is found that a multilayer feedforward neural network with three hidden layers, each including ten nodes, is the best architecture, i.e., it guarantees no overfitting in the retrieval of oil parameters from the simulated DRs. Note that the DR values ingested by the ANN are subject to data normalization. The final ANN architecture is shown in Fig. 3, where the three input neurons ($\mathrm{DR}_{\mathrm{HH}}$, $\mathrm{DR}_{\mathrm{VV}}$, and $\theta_i$) and the two output neurons ($d$ and $f_v$) are shown. In this study, the ANN is trained for the retrieval of $d$ and $f_v$ simultaneously to exploit their correlation. In fact, $d$ and $f_v$ are a joint effect on the predicted NRCS since they are both linked to the reflection properties of the composite sea surface. In addition, $d$ also affects the oil damping.

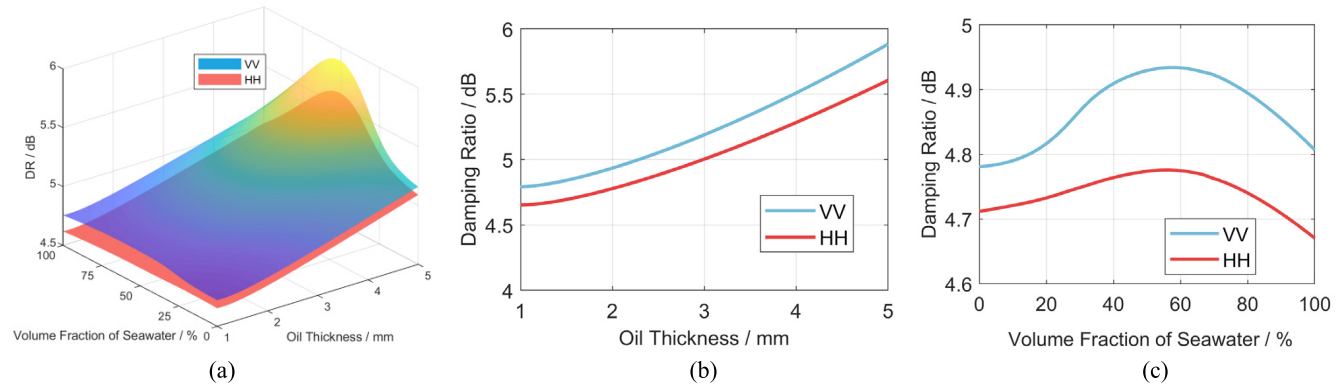


Fig. 2. (a) Predicted L-band VV (blue) and HH (red) DR values (decibel scale is adopted) versus oil thickness and seawater volume fraction. An incidence angle of 30° and a wind speed of 5 $ms^{-1}$ are considered. (b) Predicted DR values versus oil thickness for $f_v = 50\%$. (c) Predicted DR values versus seawater volume fraction when $d = 2$ mm.

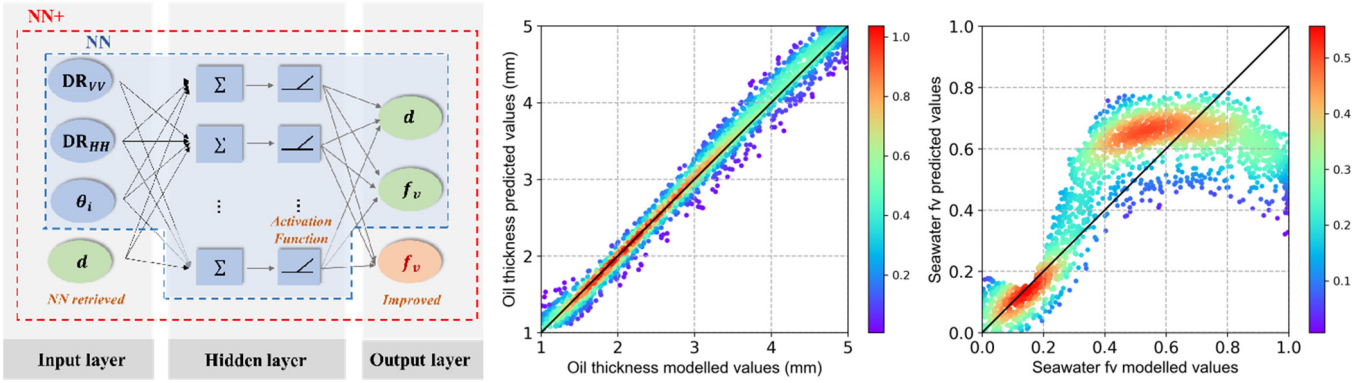


Fig. 3. (a) Sketch of the ANN structure with blue and red dashed boxes denoted NN and NN+, respectively. (b) Density plot of predicted versus modeled oil thickness values. (c) Density plot of predicted versus modeled W/O seawater volume fraction. The colormap in (b) and (c) represents the estimated Gaussian kernel density of the testing dataset multiplied by the number of testing samples with red color denoting much greater density of testing samples and blue color denoting the opposite.

The training is carried out using the resilient backpropagation algorithm. To evaluate the ANN performance and to discuss its robustness, a set of simulation samples—independent of the training process—which consists of oil parameters and corresponding DRs, is considered as a validation dataset. The early stopping is utilized to stop the training at the right time and to improve the training efficiency. Once the network is adequately trained by random data generated using the FSM, the ANN is tested on the validation dataset, for which the same normalization applied for the training dataset is adopted. The ANN output is then subjected to the inverse normalization.

The retrieved $d$ and $f_v$ values are contrasted with the corresponding modeled values from the test dataset, see the density plot of Fig. 3(b) and (c), respectively, where the $z$-axis represents the variable density estimated using a Gaussian Kernel. The scores of the inversion scheme, i.e., the coefficient of determination ($R^2$), the mean absolute error (MAE), and the mean square error (MSE), are listed in Table II. The network that deals with the oil thickness retrieval, see Fig. 3(b), has been accurately trained as can be observed by the distribution of ANN retrieved values that mostly concentrate along the 1:1 line with the FSM modeled values.

TABLE II
INVERSION SCHEME PERFORMANCE EVALUATED ON THE TEST DATASET

| Parameters | $R^2$ | RMSE | MAE | MSE |
|---|---|---|---|---|
| Oil thickness (mm) | 0.9830 | 0.1519 | 0.1148 | 0.0231 |
| Volume fraction (%) | 0.5867 | 2.7942 | 14.0300 | 3.4500 |
| Volume fraction (%) estimated using NN+ | 0.8528 | 0.1109 | 8.9400 | 1.1200 |

Quantitatively, $R^2$ is equal to about 0.98, while MAE and MSE values are about 0.11 and 0.02 mm, respectively.

The network that deals with the inversion of W/O volume fraction is fed with the same inputs of the ANN used for oil thickness retrieval (see Fig. 3(a) denoted by blue dashed box). Results, depicted in Fig. 3(c), show that the ANN results in volume fraction values, which are less consistent with the FSM ones, especially when the latter are larger than 0.3 where values inverted from the network saturate. This is quantitatively confirmed by $R^2$ that decreases to 0.59 with an MAE of about 14.03%, see Table II. This means that the trained ANN does not work properly in the retrieval of $f_v$.

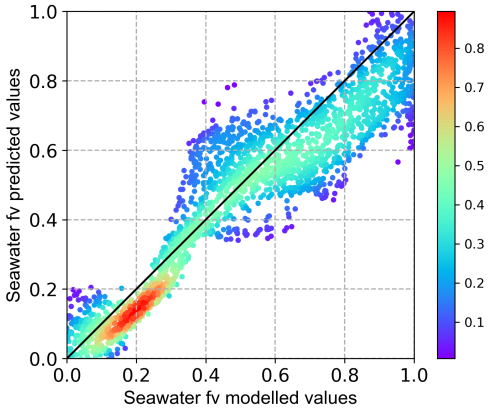


Fig. 4. Density plot of W/O seawater volume fraction retrieved by NN+ versus the one simulated with FSM.

To improve the retrieval of $f_v$, a new NN structure (NN+, see Fig. 3(a) denoted by the red dashed box) is designed where the previously retrieved $d$ is used as an input neuron. The performance NN+ on the test dataset is shown in Fig. 4 and Table II. Those results clearly demonstrate that NN+ significantly improves all the scores of the former ANN and that the distribution of $f_v$ values retrieved by NN+ is much closer to the 1:1 line with the FSM model values. By contrasting NN and NN+ density plots (see Figs. 3(c) and 4), it can be noted that NN+ improves the retrieval performance at $f_v$ around 0.4 and $f_v$ larger than 0.8 but overestimates $f_v$ values smaller than 0.4.

It must be pointed out that the ANN approach, to reduce the occurrence of multiple solutions of $d$ and $f_v$, adopts a strategy that consists of minimizing the error in the training dataset. In this way, the underestimation of inversion results for $f_v$ in the range of 0–0.4 in Fig. 4 may be at the expense of improvement of $f_v$ inversion around 0.4 and 0.8.

## IV. Experiments on Actual Airborne SAR Imagery

In this section, the proposed ANN-based retrieval approach is applied to actual polarimetric L-band airborne SAR measurements.

### A. DWH Oil Spill

The DWH oil spill in the northern part of Gulf of Mexico can be considered as the largest marine oil spill accident in the history. On 20 April 2010, the DWH drilling rig exploded causing human losses and casualties. The oil spillage has lasted for 87 days before the well was finally capped. An enormous disaster took place, which can be roughly estimated to be 3.19 million barrels (roughly 500 000 $m^3$) of oil and several hundreds and thousand tons of hydrocarbon gases released into the ocean, which caused extensive damage to marine and coastal environment, as well as the wildlife habitat and ecosystem [52]. The enormous oil slicks that formed during the accident provide an unprecedented opportunity to study oil films, characterized by unique thickness variability and spatial extent features, using remotely sensed measurements, including the ones collected by SAR [53].

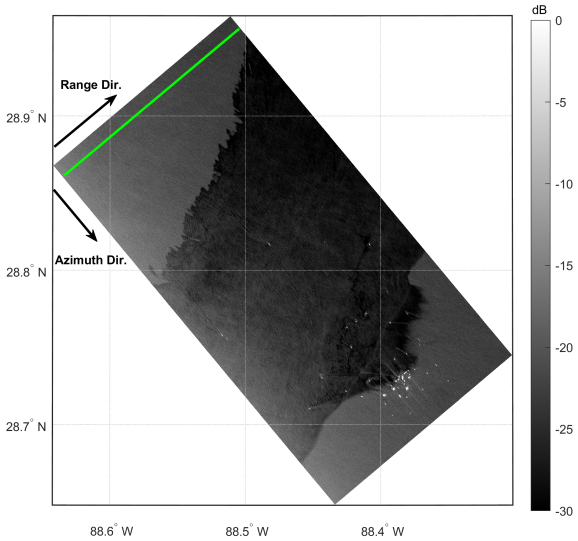


Fig. 5. VV-polarized UAVSAR image of DWH oil spill collected on June 23, 2010 at 20:42 UTC. The green line indicates the slick-free sea surface range-oriented transect considered for the quantitative analysis.

### B. UAVSAR Data

During the accident, many measurements were remotely sensed by airborne and satellite sensors over the polluted area, including the airborne UAVSAR equipped on the Gulfstream-III aircraft operated by the U.S. National Aeronautics and Space Administration (NASA). The UAVSAR is a quad-polarimetric L-band sensor with wide range and high-quality imaging capabilities (incidence angle spanning from 22° up to 65° from near to far range), i.e., a swath width of about 22 km, calling for a minimum NESZ of −54 dB [54]. During the DWH oil spill, UAVSAR acquired images of the main slick area on 22–23 June [55].

The image used in this study was collected on June 23 at 20:45 UTC, flight ID 14010, where the UAVSAR overflew the DWH rig site at a heading of 140° (filename: gulfco_14010_10054100_100623). Preprocessing is carried out that consists of multilooking (3 range × 12 azimuth looks) to get a pixel spacing of 5 × 7.2 m in slant range and azimuth. Since the oil may have undergone a weathering process, including emulsion, evaporation, and sedimentation, the characteristics of the slick exhibit significant variations from thin sheens to thicker layers of crude oil and oil emulsions. The bulk of the spilled oil imaged by the UAVSAR consists primarily of brown emulsified oil, ranging from red to brown in color, mixed with thinner (silver and rainbow) sheen layers. This analysis comes from collective observations and interpretations by trained personnel of the properties of the oil from aerial photographs [16]. At the UAVSAR acquisition time, the sea surface conditions, obtained by both buoy data and Wavewatch III model predictions, called for a wind speed between 2.5 and 5 m/s with directions from 115° to 145°.

In this study, quantitative analysis is performed on data collected at intermediate incidence angles, i.e., from 37° to 63°, to sort out pixels whose backscattering is dominated by specular mechanism and pixels whose backscattering is corrupted by noise [47]. An excerpt of the VV-polarized SAR

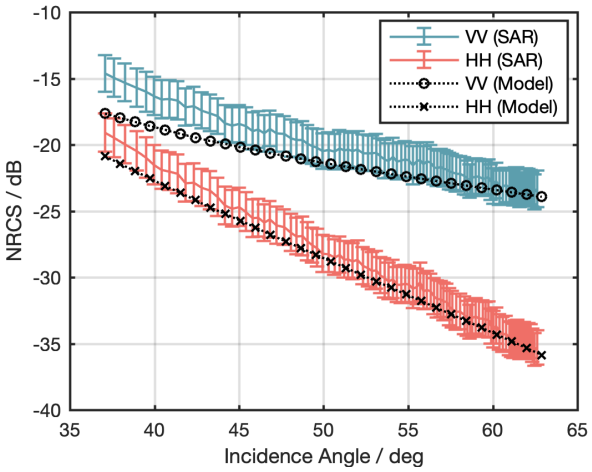


Fig. 6. NRCS versus incidence angle measured over the slick-free sea surface (see green line highlighted in Fig. 5) at VV (blue) and HH (red) polarizations. Note that AIEM predictions are also annotated in black with circle (VV) and cross (HH) markers.

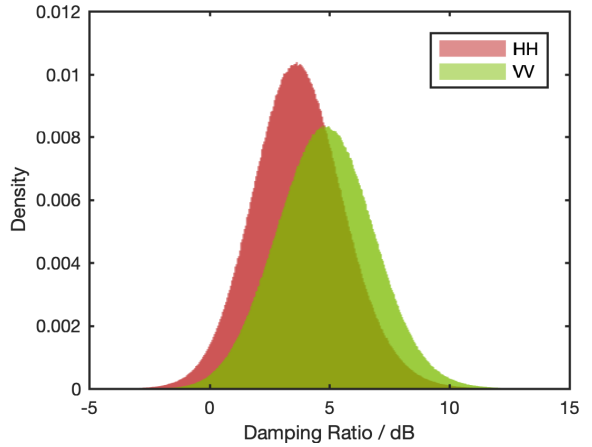


Fig. 7. Probability density function of DR values evaluated from HH (red) and VV (green) UAVSAR channels.

image that includes the oil slick is depicted, in graytones and dB scale, in Fig. 5, where several bright spots at the bottom of the slick are clearly visible that mostly refer to ships involved in cleaning-up operations.

### C. Analysis on SAR Measurements

To verify the effectiveness of the FSM in predicting the NRCS related to sea surface, the statistics of the slick-free NRCS are evaluated over the samples belonging to the green line in Fig. 5. The mean and standard deviation values of the co-polarized NRCSs, evaluated binning the NRCS using 50 pixels in the azimuth direction and 25 pixels in the range direction, are shown in Fig. 6 using the error bar format. Blue and red colors refer to VV- and HH-polarized NRCS. In addition, the VV- and HH-polarized NRCSs predicted using the AIEM are also annotated for reference purposes (see the black plots with circle and cross markers, respectively). It can be noted that measured and predicted NRCSs exhibit a fairly good agreement confirming the expected Bragg behavior in the considered incidence angle range and sea state conditions,

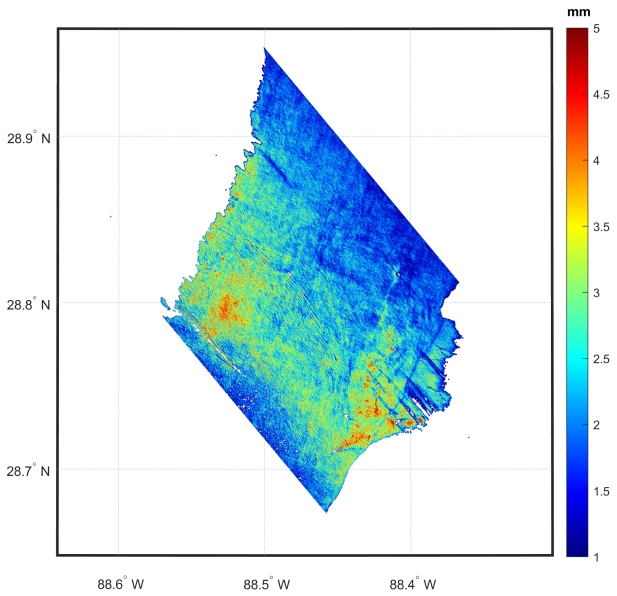


Fig. 8. Oil thickness map obtained using the ANN inversion methodology.

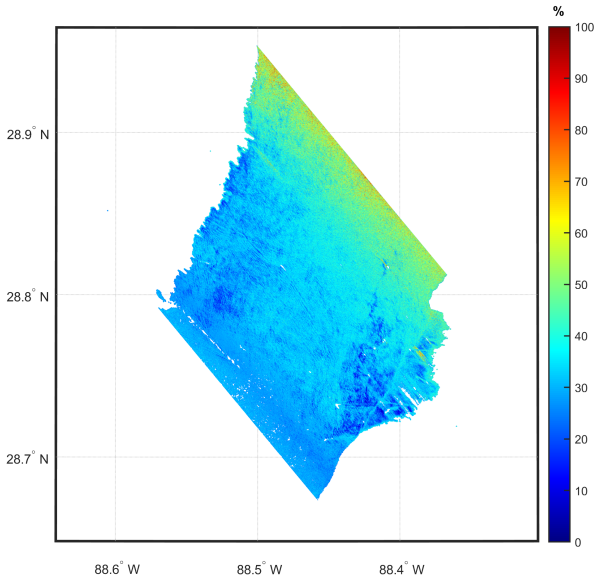


Fig. 9. Water content map obtained using the ANN inversion methodology.

i.e., the co-polarized NRCSs decrease with incidence angle and the VV channel results in larger backscattering than the HH one. However, model predictions deviate from measured NRCS values of about 2–3 (1–2) dB for VV (HH) polarization at an incidence angle of less than 45°.

The empirical probability density distribution (pdf) of HH (red) and VV (green) DR evaluated from the UAVSAR image is depicted in Fig. 7. The oil mask is obtained by applying a constant false alarm rate (CFAR) method to the VV-polarized SAR image [56]. The region of interest (ROI) of the slick-free sea surface is selected manually and the sea clutter is assumed to be Rayleigh-distributed. The false alarm rate is set as $10^{-2}$ and then the decent threshold to detect the oil slick can be obtained. To eliminate the effect of the model underestimation, the NRCS of the clean sea surface [the numerator in (12)] is derived by applying polynomial fit to mean values of the transect line in Fig. 6. Both the pdfs can be well-approximated by a normal distribution at both polarizations, with the mean value

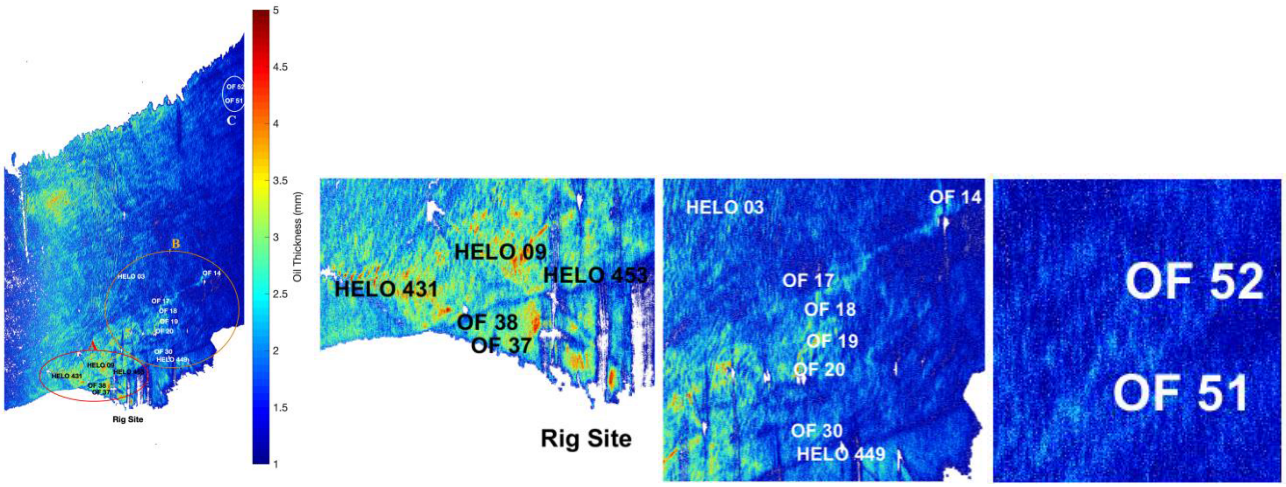


(a) (b) (c) (d)

Fig. 10. (a) ANN-based estimated oil map where ancillary photographs and observations, highlighted in Figs. 10–12, are annotated. (b) Cropping of area A. (c) Cropping of area B. (d) Cropping of area C.

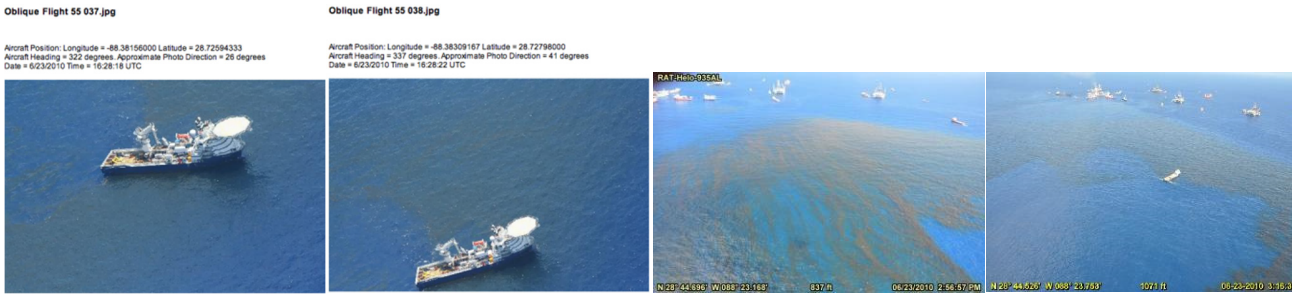


(a) (b) (c) (d)

Fig. 11. Aerial photographs collected in the area A. (First row) Images collected during the EPA ASPECT overflight oblique photography (a) 55-37: "OF 37" and (b) 55-38: "OF 38" obtained at 16:28 UTC. (Second row) Photograph collected during the RAT Helo overflight (c) "HELO 431" obtained at 19:53 UTC and (d) "HELO 453" obtained at 19:56 UTC. (Third row) Photograph collected during the TAC OPS Helo overflight "HELO 09" collected at 20:16 UTC.

about 5 (4) dB for VV (HH) polarization, with VV-polarized DR slightly stronger than that of HH-polarization as it was found in [16] and [50].

## V. Oil Parameter Retrieval From UAVSAR Data

In this section, DR evaluated from UAVSAR imagery together with the incidence angle map is ingested in the trained ANN to retrieve the oil thickness $d$ and the volume fraction of seawater $f_v$.

### A. Oil Thickness Estimation

The oil thickness estimated by applying the ANN approach to the DWH oil slick imaged by UAVSAR is depicted in Fig. 8. The thicker part is located in the south and west parts of the oil slick, which is consistent with most of the thickness pattern discussed in [4]. The estimated thickness of the thicker oil layer ranges between about 2 and 4 mm. These results agree with the visual inspections of the adsorbent pad samples collected in proximity of the DWH wellhead during the SINTEF expedition that reported an oil thickness ranging approximately between 2 and 4 mm [57]. The light brown/orange/reddish appearance of emulsions suggested that the emulsified oil was more elastic and less prone to spread over the sea surface. This indicates that the oil slick had been heavily weathered [57]. In addition, NOAA aerial observations conducted over the emulsified oil showed that the latter calls for a thickness ranging from 0.2 up to 3 mm with a mean value of 1 mm. Thinner slicks, calling for thickness smaller than 1 mm, are also present in the northeastern and southwestern parts of the slick.

### B. Volume Fraction of Seawater Estimation

The estimated volume fraction of seawater in the oil layer is depicted in Fig. 9, which shows that most of the oil slick calls for $f_v$, ranging between 20% and 30%, with an average value of about 27%. The very right portion of the slick results in the largest $f_v$, which may be due to the noise corrupting SAR measurements under high incidence angle and, therefore, making the inversion results less trustable [16]. The estimates agree with results reported in [15] where the oil volume concentration estimated by the same UAVSAR ranges from 65% up to 90% (i.e., $f_v$ ranging from 10% up to 35%) with a mean value of about 80% ($f_v$ of seawater 20%) despite a little overestimation of the mean value of $f_v$. In addition, in [15], it is shown that most of the oil was mixed with seawater at least up to a depth of a few millimeters.

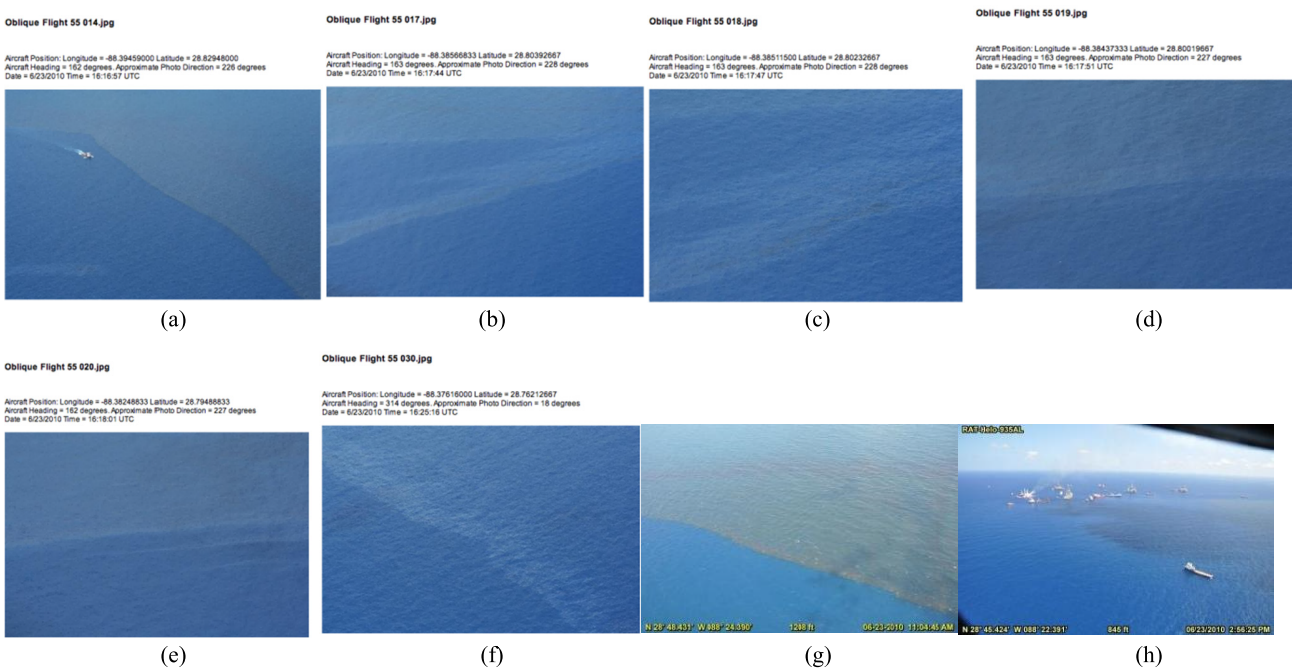


Fig. 12. Aerial photographs collected in the area B. (a)–(f) Related to oblique photography collected during the EPA ASPECT overflight "OF 14," "OF 17," "OF 18," "OF 19," "OF 20," and "OF 30" obtained between 16:16 and 16:25 UTC. (g) TAC OPS photograph acquired during the overflight "HELO 03" at 16:04 UTC. (h) Photograph taken during the RAT Helo overflight "HELO 449" obtained at 19:56 UTC.


Fig. 13. Aerial photographs collected in the area C. Oblique photography acquired during the EPA ASPECT overflight (a) "OF 51" and (b) "OF 52" at 16:49 UTC.

### C. Experimental Results Contrasted With Aerial Photographs and Visual Observations

The locations of the aerial observations are annotated on the ANN-based oil thickness map in Fig. 10. The aerial observations acquired on June 23, 2010, include NOAA aerial and helicopter imagery and observations labeled as "HELO" and Environmental Protection Agency (EPA) oblique photographs labeled as "OF." According to their locations and the ANN-based inverted thickness, the aerial data are divided into three groups (see Fig. 10): thick area, marked with a red ellipse ("area A"), middle thick area, marked with an orange ellipse (area "B"), and thin area, marked with a white ellipse (area "C"). The pictures related to aerial photographs and observations in areas A, B, and C are depicted in Figs. 11–13, respectively. Fig. 11 shows that area A calls for emulsions with red or brown appearance. Fig. 12 shows that in area B, brown emulsions together with thin sheen oils can be observed. Fig. 13 shows that in area "C," an oil–water mixing is in place with oil submerged into the seawater appearing as black stripes, which may indicate emulsions with high water content or crude oil with no water content.

## VI. Conclusion

This study is to show the feasibility of a model-based ANN approach to retrieve ancillary parameters (namely, the thickness of the oil slick and the volume fraction of seawater) related to oil spills in SAR imagery. The benefit of the proposed approach is twofold.

1) It paves the way to overcome the tremendous lack of trustable in situ measurements about oil parameters. This represents a drawback that significantly limits the use of ANN to estimate oil parameters. The approach we proposed mitigated this drawback by train the network using an FSM whose accuracy in predicting slick-free and slick-covered NRCS has been already discussed in literature.
2) The resulting model-based ANN, trained and tested by using simulated measurements, is applied to actual L-band SAR imagery that includes an oil-polluted area to retrieve the oil thickness and the fraction of water into the oil maps. Results, contrasted with independent surveys and literature studies, confirm the accuracy of the proposed approach.

In fact, by processing the L-band polarimetric radar imagery collected by the UAVSAR during the DWH oil spill accident, we found that the thicker emulsified oil—with a thickness ranging from about 2 to 4 mm—is located in the middle of the slick, while thinner films (less than 1 mm) are located at the northeastern and southwestern sides of the slick. In addition, it is found that the DWH slick is a water-in-oil mixture where the percentage of seawater ranges between about 20% and 30%. Those results agree with independent studies carried

out in [15], [16], and [57] and with areal and helicopter photographs taken by NOAA.

Although the model-based ANN showed very promising results, there is still room for improvements in both the NN architecture and the simulation of the parameters that will be addressed in future work.

## REFERENCES


[1] O. Garcia-Pineda, I. R. MacDonald, X. Li, C. R. Jackson, and W. G. Pichel, "Oil spill mapping and measurement in the Gulf of Mexico with textural classifier neural network algorithm (TCNNA)," *IEEE J. Sel. Topics Appl. Earth Observ. Remote Sens.*, vol. 6, no. 6, pp. 2517–2525, Dec. 2013.

[2] M. Fingas, "The challenges of remotely measuring oil slick thickness," *Remote Sens.*, vol. 10, no. 2, p. 319, Feb. 2018.

[3] O. Boisot, S. Angelliaume, and C.-A. Guérin, "Marine oil slicks quantification from L-band dual-polarization SAR imagery," *IEEE Trans. Geosci. Remote Sens.*, vol. 57, no. 4, pp. 2187–2197, Apr. 2019.

[4] M. Gade, H. Hühnerfuss, and G. Korenowski, *Marine Surface Films*. Amsterdam, The Netherlands: Springer, 2006.

[5] M. Fingas and C. Brown, "A review of oil spill remote sensing," *Sensors*, vol. 18, no. 2, p. 91, Dec. 2017.

[6] M. Fingas, "How to measure slick thickness (or not)," in *Proc. 35th Arctic Mar. Oil Spill Program Tech. Seminar*, 2012, pp. 617–652.

[7] C. Jones and B. Holt, "Experimental L-band airborne SAR for oil spill response at sea and in coastal waters," *Sensors*, vol. 18, no. 2, p. 641, Feb. 2018.

[8] W. Alpers, B. Holt, and K. Zeng, "Oil spill detection by imaging radars: Challenges and pitfalls," *Remote Sens. Environ.*, vol. 201, pp. 133–147, Nov. 2017.

[9] B. A. Secretariat, *Bonn Agreement Aerial Operations Handbook*, 2017. [Online]. Available: https://www.bonnagreement.org/publications

[10] J. Svejkovsky, M. Hess, J. Muskat, T. J. Nedwed, J. McCall, and O. Garcia, "Characterization of surface oil thickness distribution patterns observed during the deepwater horizon (MC-252) oil spill with aerial and satellite remote sensing," *Mar. Pollut. Bull.*, vol. 110, no. 1, pp. 162–176, Sep. 2016.

[11] M. M. Espeseth, C. E. Jones, B. Holt, C. Brekke, and S. Skrunes, "Oil-spill-response-oriented information products derived from a rapid-repeat time series of SAR images," *IEEE J. Sel. Topics Appl. Earth Observ. Remote Sens.*, vol. 13, pp. 3448–3461, 2020.

[12] T. Meng, K.-S. Chen, X. Yang, F. Nunziata, D. Xie, and A. Buono, "Simulation and analysis of bistatic radar scattering from oil-covered sea surface," *IEEE Trans. Geosci. Remote Sens.*, vol. 60, 2022, Art. no. 2003915.

[13] M. Gade, W. Alpers, H. Hühnerfuss, H. Masuko, and T. Kobayashi, "Imaging of biogenic and anthropogenic ocean surface films by the multifrequency/multipolarization SIR-C/X-SAR," *J. Geophys. Res., Oceans*, vol. 103, no. C9, pp. 18851–18866, 1998.

[14] M. Gade, W. Alpers, H. Hühnerfuss, V. Wismann, and P. Lange, "On the reduction of the radar backscatter by oceanic surface films: Scatterometer measurements and their theoretical interpretation," *Remote Sens. Environ.*, vol. 66, no. 1, pp. 52–70, Oct. 1998.

[15] B. Minchew, "Determining the mixing of oil and sea water using polarimetric synthetic aperture radar," *Geophys. Res. Lett.*, vol. 39, no. 16, 2012, doi: 10.1029/2012GL052304.

[16] B. Minchew, C. E. Jones, and B. Holt, "Polarimetric analysis of backscatter from the deepwater horizon oil spill using L-band synthetic aperture radar," *IEEE Trans. Geosci. Remote Sens.*, vol. 50, no. 10, pp. 3812–3830, Oct. 2012.

[17] S. Skrunes, C. Brekke, and T. Eltoft, "Characterization of marine surface slicks by Radarsat-2 multipolarization features," *IEEE Trans. Geosci. Remote Sens.*, vol. 52, no. 9, pp. 5302–5319, Sep. 2014.

[18] S. Skrunes, C. Brekke, T. Eltoft, and V. Kudryavtsev, "Comparing near-coincident C- and X-band SAR acquisitions of marine oil spills," *IEEE Trans. Geosci. Remote Sens.*, vol. 53, no. 4, pp. 1958–1975, Apr. 2015.

[19] S. Skrunes, C. Brekke, C. E. Jones, M. M. Espeseth, and B. Holt, "Effect of wind direction and incidence angle on polarimetric SAR observations of slicked and unslicked sea surfaces," *Remote Sens. Environ.*, vol. 213, pp. 73–91, Aug. 2018.

[20] V. Wismann, M. Gade, W. Alpers, and H. Huhnerfuss, "Radar signatures of marine mineral oil spills measured by an airborne multi-frequency radar," *Int. J. Remote Sens.*, vol. 19, no. 18, pp. 3607–3623, Dec. 1998.

[21] B. Jones, "A comparison of visual observations of surface oil with synthetic aperture radar imagery of the sea empress oil spill," *Int. J. Remote Sens.*, vol. 22, no. 9, pp. 1619–1638, Jun. 2001.

[22] S. Skrunes, A. M. Johansson, and C. Brekke, "Synthetic aperture radar remote sensing of operational platform produced water releases," *Remote Sens.*, vol. 11, no. 23, p. 2882, Dec. 2019.

[23] C. Quigley, A. M. Johansson, and C. E. Jones, "An investigation on the damping ratio of marine oil slicks in synthetic aperture radar imagery," *IEEE J. Sel. Topics Appl. Earth Observ. Remote Sens.*, vol. 16, pp. 5488–5501, 2023.

[24] C. E. Jones, "An automated algorithm for calculating the ocean contrast in support of oil spill response," *Mar. Pollut. Bull.*, vol. 191, Jun. 2023, Art. no. 114952.

[25] I. R. MacDonald et al., "Natural and unnatural oil slicks in the Gulf of Mexico," *J. Geophys. Res., Oceans*, vol. 120, no. 12, pp. 8364–8380, 2015.

[26] S. Angelliaume, O. Boisot, and C.-A. Guérin, "Dual-polarized L-band SAR imagery for temporal monitoring of marine oil slick concentration," *Remote Sens.*, vol. 10, no. 7, p. 1012, Jun. 2018.

[27] L. Zhang and L. Zhang, "Artificial intelligence for remote sensing data analysis: A review of challenges and opportunities," *IEEE Geosci. Remote Sens. Mag.*, vol. 10, no. 2, pp. 270–294, Jun. 2022.

[28] H. Adab, R. Morbidelli, C. Saltalippi, M. Moradian, and G. A. F. Ghalhari, "Machine learning to estimate surface soil moisture from remote sensing data," *Water*, vol. 12, no. 11, p. 3223, Nov. 2020.

[29] H. Chen, V. Chandrasekar, R. Cifelli, and P. Xie, "A machine learning system for precipitation estimation using satellite and ground radar network observations," *IEEE Trans. Geosci. Remote Sens.*, vol. 58, no. 2, pp. 982–994, Feb. 2020.

[30] X. Wang, J. Huang, Q. Feng, and D. Yin, "Winter wheat yield prediction at county level and uncertainty analysis in main wheat-producing regions of China with deep learning approaches," *Remote Sens.*, vol. 12, no. 11, p. 1744, May 2020.

[31] B. Janga, G. P. Asamani, Z. Sun, and N. Cristea, "A review of practical AI for remote sensing in Earth sciences," *Remote Sens.*, vol. 15, no. 16, p. 4112, 2023.

[32] Q. Yuan et al., "Deep learning in environmental remote sensing: Achievements and challenges," *Remote Sens. Environ.*, vol. 241, May 2020, Art. no. 111716.

[33] T. Meng, F. Nunziata, and X. Yang, "Model-based oil slick thickness estimation using artificial neural network," in *Proc. IEEE Int. Geosci. Remote Sens. Symp. (IGARSS)*, Jul. 2023, pp. 3994–3997.

[34] T. Meng, X. Yang, K.-S. Chen, F. Nunziata, D. Xie, and A. Buono, "Radar backscattering over sea surface oil emulsions: Simulation and observation," *IEEE Trans. Geosci. Remote Sens.*, vol. 60, 2022, Art. no. 2000714.

[35] D. Xie, K.-S. Chen, and X. Yang, "Effects of wind wave spectra on radar backscatter from sea surface at different microwave bands: A numerical study," *IEEE Trans. Geosci. Remote Sens.*, vol. 57, no. 9, pp. 6325–6334, Sep. 2019.

[36] D. Xie, K.-S. Chen, and J. Zeng, "The frequency selective effect of radar backscattering from multiscale sea surface," *Remote Sens.*, vol. 11, no. 2, p. 160, Jan. 2019.

[37] K. S. Chen, T.-D. Wu, L. Tsang, Q. Li, J. Shi, and A. K. Fung, "Emission of rough surfaces calculated by the integral equation method with comparison to three-dimensional moment method simulations," *IEEE Trans. Geosci. Remote Sens.*, vol. 41, no. 1, pp. 90–101, Jan. 2003.

[38] A. K. Fung, Z. Li, and K. S. Chen, "Backscattering from a randomly rough dielectric surface," *IEEE Trans. Geosci. Remote Sens.*, vol. 30, no. 2, pp. 356–369, Mar. 1992.

[39] T. Elfouhaily, B. Chapron, K. Katsaros, and D. Vandemark, "A unified directional spectrum for long and short wind-driven waves," *J. Geophys. Res., Oceans*, vol. 102, no. C7, pp. 15781–15796, 1997.

[40] C. A. Balanis, *Advanced Engineering Electromagnetics*. Hoboken, NJ, USA: Wiley, 2012.

[41] O. Garcia-Pineda et al., "Classification of oil spill by thicknesses using multiple remote sensors," *Remote Sens. Environ.*, vol. 236, Jan. 2020, Art. no. 111421.

[42] V. Corcione, A. Buono, F. Nunziata, and M. Migliaccio, "A sensitivity analysis on the spectral signatures of low-backscattering sea areas in Sentinel-1 SAR images," *Remote Sens.*, vol. 13, no. 6, p. 1183, Mar. 2021.

[43] M. F. Fingas and C. E. Brown, "Review of oil spill remote sensing," *Spill Sci. Technol. Bull.*, vol. 4, no. 4, pp. 199–208, Jan. 1997.

[44] W. Alpers and H. Hühnerfuss, "The damping of ocean waves by surface films: A new look at an old problem," *J. Geophys. Res.*, vol. 94, no. 5, pp. 6251–6265, May 1989.
[45] A. D. Jenkins and S. J. Jacobs, "Wave damping by a thin layer of viscous fluid," *Phys. Fluids*, vol. 9, no. 5, pp. 1256–1264, May 1997.
[46] I. Sergievskaya, S. Ermakov, T. Lazareva, and J. Guo, "Damping of surface waves due to crude oil/oil emulsion films on water," *Mar. Pollut. Bull.*, vol. 146, pp. 206–214, Sep. 2019.
[47] A. H. Sihvola, *Electromagnetic Mixing Formulas and Applications*, no. 47. Edison, NJ, USA: IET, 1999.
[48] F. T. Ulaby et al., *Microwave Radar and Radiometric Remote Sensing*, no. 5. Ann Arbor, MI, USA: Univ. Michigan Press 2014.
[49] A. Montuori, F. Nunziata, M. Migliaccio, and P. Sobieski, "X-band two-scale sea surface scattering model to predict the contrast due to an oil slick," *IEEE J. Sel. Topics Appl. Earth Observ. Remote Sens.*, vol. 9, no. 11, pp. 4970–4978, Nov. 2016.
[50] N. Pinel, C. Bourlier, and I. Sergievskaya, "Two-dimensional radar backscattering modeling of oil slicks at sea based on the model of local balance: Validation of two asymptotic techniques for thick films," *IEEE Trans. Geosci. Remote Sens.*, vol. 52, no. 5, pp. 2326–2338, May 2014.
[51] Ö. Ceyhun and A. Yalçın, "Remote sensing of water depths in shallow waters via artificial neural networks," *Estuarine, Coastal Shelf Sci.*, vol. 89, no. 1, pp. 89–96, Sep. 2010.
[52] J. Beyer, H. C. Trannum, T. Bakke, P. V. Hodson, and T. K. Collier, "Environmental effects of the Deepwater Horizon oil spill: A review," *Mar. Pollut. Bull.*, vol. 110, no. 1, pp. 28–51, 2016.
[53] D. Latini, F. Del Frate, and C. E. Jones, "Multi-frequency and polarimetric quantitative analysis of the Gulf of Mexico oil spill event comparing different SAR systems," *Remote Sens. Environ.*, vol. 183, pp. 26–42, Sep. 2016.
[54] S. Angelliaume, B. Minchew, S. Chataing, P. Martineau, and V. Miegebielle, "Multifrequency radar imagery and characterization of hazardous and noxious substances at sea," *IEEE Trans. Geosci. Remote Sens.*, vol. 55, no. 5, pp. 3051–3066, May 2017.
[55] M. Migliaccio and F. Nunziata, "On the exploitation of polarimetric SAR data to map damping properties of the deepwater horizon oil spill," *Int. J. Remote Sens.*, vol. 35, no. 10, pp. 3499–3519, May 2014.
[56] E. Ferrentino, F. Nunziata, A. Buono, A. Urciuoli, and M. Migliaccio, "Multipolarization time series of Sentinel-1 SAR imagery to analyze variations of Reservoirs' water body," *IEEE J. Sel. Topics Appl. Earth Observ. Remote Sens.*, vol. 13, pp. 840–846, 2020.
[57] O. Garcia-Pineda et al., "Detection of floating oil anomalies from the deepwater horizon oil spill with synthetic aperture radar," *Oceanography*, vol. 26, no. 2, pp. 124–137, Jun. 2013.

**Tingyu Meng** (Associate Member, IEEE) received the B.S. degree in remote sensing science and technology from Wuhan University, Wuhan, China, in 2018, and the Ph.D. degree in cartography and geographic information systems from the Aerospace Research Institute, Chinese Academy of Sciences (AIRCAS), Beijing, China, in 2023.

She is currently a Research Associate with the National Key Laboratory of Microwave Imaging Technology, AIRCAS. Her research interests include marine remote sensing, synthetic aperture radar (SAR) applications in lunar exploration, and modeling of electromagnetic scattering.

**Ferdinando Nunziata** (Senior Member, IEEE) was born in Avellino, Italy, in 1982. He received the B.Sc., M.Sc., and Ph.D. degrees in telecommunication engineering from the Università degli Studi di Napoli "Parthenope," Naples, Italy, in 2003, 2005, and 2008, respectively.

Since 2019, he has been an Associate Professor with the Università degli Studi di Napoli "Parthenope." His main research interests include applied electromagnetics, i.e., sea surface scattering, radar polarimetry, synthetic aperture radar (SAR) sea oil slick and metallic target monitoring, spatial resolution enhancement techniques, and global navigation satellite system reflectometry (GNSS-R).

**Xiaofeng Yang** (Senior Member, IEEE) received the B.S. degree in environmental science from Sichuan University, Chengdu, China, in 2005, and the Ph.D. degree in cartography and geographic information systems from the Institute of Remote Sensing Applications (IRSA), Chinese Academy of Sciences (CAS), Beijing, China, in 2010.

From 2009 to 2010, he was a Visiting Research Scientist with the Department of Atmospheric and Oceanic Science, University of Maryland, College Park, MD, USA. In 2010, he joined IRSA, CAS, where he became an Associate Professor in 2013 and a Full Professor in 2016. Since 2024, he has been a Full Professor with Nanjing University, Suzhou Campus, Suzhou, China. His research interests include satellite oceanography, synthetic aperture radar (SAR) remote sensing, and marine atmospheric boundary layer process studies.

Dr. Yang is an Associate Editor of IEEE TRANSACTIONS ON GEOSCIENCE AND REMOTE SENSING. He is the Secretary of the Technical Committee on Earth Science from Space, Chinese Society of Space Research.

**Andrea Buono** (Senior Member, IEEE) was born in Naples, Italy, in 1984. He received the B.Sc. and M.Sc. degrees in telecommunication engineering from the Università degli Studi di Napoli "Parthenope," Naples, in 2010 and 2013, respectively, and the Ph.D. degree in information engineering from the Università di Napoli "Parthenope," Naples, in 2017.

Since 2018, he has been an Assistant Professor in electromagnetics with the Università degli Studi di Napoli "Parthenope." His main research activities deal with applied electromagnetics, including electromagnetic modeling, polarimetry, ocean, and coastal area applications.

**Kun-Shan Chen** (Fellow, IEEE) received the Ph.D. degree in electrical engineering from The University of Texas at Arlington, Arlington, TX, USA, in 1990.

From 1992 to 2014, he was a Professor with National Central University, Taoyuan, Taiwan. From 2014 to 2024, he was with the Institute of Remote Sensing and Digital Earth, Chinese Academy of Sciences, Beijing, China, and Guilin University of Technology, Guilin, China. He joined the Institute of Space Earth Science, Nanjing University, Suzhou, China. He has authored and coauthored over 400 referred journal articles and conference papers and contributed ten book chapters. He is the coauthor of five books. His research interests include microwave remote sensing theory, modeling, system and measurement, and electromagnetic sensing techniques.

Dr. Chen is a member of the Academia Europaea. He was the IEEE GRSS Adcom Member from 2010 to 2014. He received the 2021 IEEE GRSS Fawwaz Ulaby Distinguished Achievement Award. He was the Founding Chair of the GRSS Taipei Chapter. He was the Co-Chair of the Technical Committee for IGARSS 2016, IGARSS2017, and IGARSS 2020. His academic activities include as a Deputy Editor-in-Chief of IEEE TRANSACTIONS ON GEOSCIENCE AND REMOTE SENSING and the Founding Deputy Editor-in-Chief of IEEE JOURNAL OF SELECTED TOPICS IN APPLIED EARTH OBSERVATIONS AND REMOTE SENSING from 2008 to 2010, He has been a member of the Editorial Board of the PROCEEDINGS OF THE IEEE from 2014 to 2019. He has been an Editorial Board Member of IEEE ACCESS since 2020.

**Maurizio Migliaccio** (Fellow, IEEE) was born in Naples, Italy, in 1962. He received the Laurea degree (Hons.) in electronic engineering from the Università di Napoli Federico II, Naples, in 1987.

He is currently a Full Professor of electromagnetics with the Università degli Studi di Napoli "Parthenope," Naples. His scientific interests include remote sensing for marine and coastal applications, polarimetry, inverse problem for resolution enhancement, and reverberating chambers.